



# Lath martensite substructure evolution in low-carbon microalloyed steels

Arnab Chakraborty<sup>1</sup>, Richard F. Webster<sup>2</sup>, and Sophie Primig<sup>1,\*</sup>

<sup>1</sup>School of Materials Science & Engineering, UNSW Sydney, Kensington, NSW 2052, Australia

<sup>2</sup>Mark Wainwright Analytical Centre, UNSW Sydney, Kensington, NSW 2052, Australia

Received: 23 February 2022

Accepted: 27 April 2022

Published online:  
18 May 2022

© The Author(s) 2022

## ABSTRACT

Lath martensite substructures in as-quenched plain carbon steels exhibit dislocation-like contrast in the transmission electron microscope. More recent observations reported internal twins and nanoscale auto-tempered intra-lath carbides as additional lath substructures in ultra-low-C binary Fe–C steels. Modern microalloyed steels often have similar ultra-low C contents besides microalloying elements like Ti, Nb or V and, more recently, Mo, to achieve high strength, toughness and weldability. Nonetheless, little is known about the lath substructure evolution in the as-quenched state of microalloyed steels. This study investigates the hierarchical martensite substructure evolution post-quenching of microalloyed Nb and NbMo steels with 0.1 wt% C. Hierarchical microstructure characterization was done using scanning and transmission electron microscopy, and electron backscatter diffraction methods including parent grain reconstructions with MTEX. Thermokinetic simulations using MatCalc to determine the carbide evolution during auto-tempering were corroborated with site-specific transmission electron microscopy. Mo addition led to lowering of the martensite start temperature, yet the Nb steel showed a finer hierarchical microstructure. Finer laths with in-lath dislocations, short and long twins, and lath boundary decoration of carbides were found in the Nb steel. Conversely, laths in the NbMo were wider, with frequent intra-lath auto-tempered precipitates in the vicinity of dislocations, without twins.

## Introduction

Lath martensite is known to form during quenching of low- to medium-carbon steels with nominal carbon contents below 0.6 wt% in plain Fe–C steels following

austenitization [1]. The crystal structure of lath martensite in low-carbon (< 0.2 wt% C) steels is body-centered cubic (bcc) similar to ferrite ( $\alpha$ ), owing to minimal tetragonality due to the low nominal carbon contents [2]. A comprehensive study of hierarchical microstructural units for low-C steels by

Handling Editor: Catalin Croitoru.

Address correspondence to E-mail: s.primig@unsw.edu.au

<https://doi.org/10.1007/s10853-022-07275-9>

Maki et al. [3] observed clusters of parallel laths sharing common habit planes arranged into packets. These packets are further subdivided into 'blocks' of laths. While a martensite lath is a single crystal with lattice defects, a block is an aggregation of laths having the same crystal orientation, often comprising of pairs of laths termed variants. The packets are collections of blocks with the same  $\{111\}_\gamma$  plane. Individual packets of lath martensite are in turn arranged within prior austenite grains (PAGs), having specific boundary misorientations based on the orientation relationships assumed during the austenite ( $\gamma$ ) to  $\alpha$  transformation. Because there are four different  $\{111\}_\gamma$  planes, there can only be four different packets formed while as many as 24 possible variants of lath martensite may form inside every PAG [4–7]. Furthermore, packet and block boundaries are high-angle boundaries, while lath boundaries exhibit low misorientations, forming low-angle boundaries. Similar observations of hierarchical martensite microstructures were also made in previous studies for a wide range of low-C, Fe–C and Fe–Ni martensites [1, 4, 7–10].

Prior studies assessing the microstructure of as-quenched martensitic steels have predominantly focused on the effects of nominal carbon content, prior austenite grain size, packet and block size, and effective lath width on the overall strength of martensite [3, 6, 8, 10–13]. These studies observed that the high-angle boundaries of packets and blocks restrict slip transmission and, thus, are known to be effective strengthening contributors as observed previously by many authors [5, 12–17]. However, little is known about the lath substructural evolution in as-quenched low-carbon microalloyed martensitic steels [18]. Martensitic transformations follow a displacive mechanism which invariably results in the generation of transformation induced plasticity. This introduces dislocations and may promote twinning within the matrix, depending on the steel composition [19].

Studies by Tan et al. [20] observed the evolution of internally twinned martensite plates as predominant substructure in plain and high-carbon as-quenched steels while others [1, 3, 21] reported lath martensite substructures exhibiting a high density of tangled dislocations with essentially no fine twins in low-carbon Fe-based alloys. More recent studies on lath substructures in binary Fe-0.02–0.05% C steels (all compositions in wt% in the following) by Ping et al.

[22] reported fine auto-tempered carbides of a few tens of nanometers in width, identified as  $\omega$ -Fe(C) particles at twin boundaries, inside laths. Interestingly, two types of twins defined as *short* and *long* twins [23] as lath martensite substructures were frequently observed in a Fe-0.05% C steel when quenched from austenitization temperatures between 1050 and 1200 °C. Ping et al. [23] further reported observing auto-tempered transition carbides at  $\{112\} < 111 >$ -bcc-type twin boundaries in an Fe-0.1C steel. In situ tempering treatment of initially austenitized and water-quenched Fe-0.2% C steel foils by Man et al. [24] revealed a transition from a predominantly twinned lath substructures to a predominantly dislocation contrast-like substructure.

Lath substructures further play a key role in determining final properties of martensitic steels by influencing the mobility of interstitial and substitutional alloying elements. Hutchinson et al. [25] observed an increase in C segregation to both lath boundaries and dislocations inside laths with increasing C content for commercial deformed and quenched 0.1–0.5% C steels. They concluded that the segregation of C to these defects must be the main factor in contributing to the hardness of as-quenched martensite in low-C steels. Moreover, Badiner et al. [14] reported substructural heterogeneity with lath width variations in controlling the evolution of dislocation density, thereby influencing the overall martensite strength in a 0.39C–0.65Mn–0.34Mo–0.72Cr–1.4Ni–1.67Si quenched and tempered steel. The dislocation density variation effectively influences the mobility of solute C segregation at these defect regions, thereby influencing the overall solute C available in solid solution for further precipitation during tempering treatments between 120 and 150 °C.

High-strength steels with a martensitic matrix are important engineering materials for structural components in the automotive and line-pipe industries [26–28]. Conventionally, Nb microalloyed steels are ideal grades for such high-strength applications, although more recently advances in alloy design [29–33] resulted in processing of ultra-low-C microalloyed steels with Mo additions to further improve yield strength, toughness and weldability properties. While these previous studies have focused on the influence of alloying and hierarchical unit sizes on the martensitic strength, little is known

about the lath microstructure evolution in the as-quenched state such steels.

Thus, the aim of the present work is to examine the lath substructure evolution in two low-C microalloyed Nb steels, with focus on the role of Mo. For this purpose, quench dilatometer experiments were performed on model Nb and NbMo steels with 0.1% C, underpinned by thermokinetic simulations determining martensite transformation kinetics and auto-tempered carbide size distributions using the software MatCalc. Thorough microstructural characterization of as-quenched steels including scanning electron microscopy, electron backscatter diffraction and site-specific transmission electron microscopy were conducted to reveal the evolving lath substructures.

## Materials and methods

Two model microalloyed steels were prepared using a vacuum induction furnace INDUTHERM VTC200 following multiple Ar purge cycles prior to melting and casting. For more details about the preparation of these steels, please refer to [33]. The chemical compositions of the castings were evaluated using inductively coupled plasma mass spectroscopy technique and were reported to be (in wt%) 0.1C–1.45Mn–0.20Si–0.04Nb (Nb steel) and 0.1C–1.48Mn–0.16Si–0.05Nb–0.23Mo (NbMo steel). Standard hollow cylindrical quench dilatometer samples with outer and inner diameters of 4 mm and 2 mm, respectively, with an overall length of 10 mm were prepared. Austenitization followed by Ar-quenching was performed in a TA instruments DIL 805A quench dilatometer. For temperature measurements, a type B thermocouple was spot welded to the sample surfaces and quartz (SiO<sub>2</sub>) push rods recorded the dilatations. The samples were heated at 5 °C/s to an austenitization temperature of 1215 °C and held under vacuum for 120 s followed by Ar-quenching at average cooling rates exceeding 100 °C/s. The austenitization parameters were selected based on complete dissolution of any carbides present in the pre-materials of both the Nb and NbMo steels as predicted by MatCalc. The heat rate is a typical industrially achievable one. Successively, the martensite start ( $M_s$ ) and finish ( $M_f$ ) temperatures were evaluated from slope deviations in the dilatation versus cooling temperature plots for each steel,

following the method described by Kaar et al. [34]. To determine the transformed volume fraction of martensite from dilatometry experiments, the well-known lever rule was employed [35].

The experimentally determined  $M_s$  temperatures were further validated by thermokinetic simulations using MatCalc (v6.03, rel. 0.017) with built-in thermodynamic and diffusion databases for Fe (mc\_fe.tdb). These simulations were based on initial evaluations of variations in  $T_0$  temperatures (i.e., for identical chemical composition, the molar Gibbs energy for austenite and ferrite are equal at  $T_0$ ) as a function of C content. However, additional driving forces are necessary to initiate the martensitic transformation below the  $T_0$  temperature. Based on previous studies on the role of Mo on the resistance against transformation due to localized strengthening to accommodate plastic strains [36], slightly higher driving force values were assumed for the  $M_s$  temperature simulations of the NbMo steel (1700 J/mol) compared to the Nb steel (1200 J/mol). MatCalc was further used to predict size class distributions of cementite precipitated due to auto-tempering. For this purpose, the cementite kinetics simulations from previous work by Zamberger et al. [37] were adopted.

Metallographic preparation of the as-quenched microstructures included mechanical grinding and diamond slurry polishing followed by etching with 2% Nital solution for imaging in a Schottky field emission scanning electron microscope (SEM) JEOL 7001F operated at 20 kV. Lath microstructures were more closely examined under backscattered imaging conditions in the same microscope which was also equipped with a high-speed Hikari-EDAX camera for electron backscattered diffraction (EBSD).

For EBSD investigations, polished samples were further finish-polished with 0.03 μm Si oxide suspension (OP-U) to relieve surface stresses from prior mechanical polishing. EBSD scans of 150 × 150 μm<sup>2</sup> and 80 × 80 μm<sup>2</sup> map areas with a step size of 0.1 μm were used for hierarchical microstructural analyses (block sizes), while larger area scans of 400 × 400 μm<sup>2</sup> were used for reconstructions of prior austenite grains. All scans were done using a binning of 5 × 5 under an acceleration voltage of 20 kV at a working distance of 15 mm. Post-scanning EBSD data analyses were performed using the TSL OIM v8.0 software. EBSD data cleanup for evaluation of the PAG sizes included a grain dilation step, while the overall area

analyses in scanned regions were performed under a confidence index value of  $> 0.1$  to eliminate unindexed points. For analyses of the block sizes, further cleanup steps included associating aggregates of measured points surrounded by high-angle boundaries with misorientations  $> 15^\circ$ . To minimize the influence of misindexed points, the minimum number of measured points used for constructing individual grains was set to three.

The cleaned-EBSD scan data ( $400 \times 400 \mu\text{m}^2$  maps) were exported into (.ang) file format as input files for a MATLAB-based script used to compute PAG sizes. This computation was done with the help of an open-source crystallographic toolbox (MTEX v5.7.1) with the add-on software ORTools (rel. 1.1.2) [38]. The ability of MTEX to calculate existing irrational orientation relationships (OR) from input EBSD data results in highly accurate identification of PAG. This irrational OR often falls in between the rational K-S and Nishiyama–Wassermann ORs in lath martensite. Successful PAG reconstruction using ORtools scripts involves identifying parent boundary regions with  $< 5^\circ$  misorientation as regions sharing a common parent austenite orientation [38]. Finally, a quantitative estimate of the PAG size from reconstructed maps using the linear intercept method is performed. Additionally, it was ensured the intercept evaluation did not include twin boundaries inside individual PAGs. By default, MTEX assigns the numbering of packets and variants as established by Morito et al. [12] for cube–cube ( $\gamma$ - $\alpha'$ ) symmetrical transformations.

For transmission electron microscopy (TEM) analyses of lath substructures, site-specific samples were lifted out and attached to Cu grids by focused ion-beam milling within identifiable PAGs using a Thermo-Fisher Helios G4 PFIB dual beam microscope following a method developed by Tomus et al. [39]. TEM studies were then conducted using a cold-field emission JEOL-F200 operated at 200 kV. This was done after a final Ar<sup>+</sup> ion milling in a Fischione Nanomill gentle clean of the lift-out lamellae performed at 500 eV for 10 min at  $10^\circ$  on each side to remove ion-milling artifacts such as Pt/Ga deposition. The TEM used was equipped with a JEOL 100 mm<sup>2</sup> silicon-drift X-ray detector with a collection angle of close to 1 sr used for energy-dispersive spectroscopy (EDS) line scans.

## Results

### Dilatation test and as-quenched microstructures

#### *Martensite start temperature evaluation*

The dilatation strain versus cooling temperature profile for both steels is shown in Fig. 1a. An enlarged region of the plot recording the martensite start ( $M_s$ ) and finish ( $M_f$ ) temperatures during cooling is shown in Fig. 1b.

Sharp slope deviations were recorded at temperatures being consistent with  $M_s$  temperatures for other low-C steels during rapid quenching [40]. Figure 1b shows that the Nb steel shows a higher  $M_s$  temperature of  $494^\circ\text{C}$ , while the a lower  $M_s$  of  $417^\circ\text{C}$  was recorded for the NbMo steel. The  $M_f$  temperatures were recorded as  $401^\circ\text{C}$  for the Nb steel and  $386^\circ\text{C}$  for the NbMo steel. Additional dilatometry measurements across wide range of cooling rates are presented in Supplementary Fig. 1, which provide further evidence for the influence of 0.23% Mo in lowering of the phase transformation starting temperatures under cooling.

Furthermore, the dilatation–cooling profile between the  $M_s$  and the  $M_f$  temperatures appeared to be narrower for the NbMo steel when compared to broader range of transformation temperatures for the Nb steel. This implies variation in the amount of initial martensite formed within this range. This is believed to accordingly influence the overall martensitic transformation kinetics and final lath substructure evolution as discussed in the following sections.

#### *As-quenched microstructures*

The as-quenched microstructures from the dilatation test are shown in Fig. 2, revealing a fully martensitic matrix for both the steels. Figure 2a, b shows the SEM micrographs of Nb and NbMo steels, respectively, with laths (white arrows) within individual prior austenite grains, with their boundaries depicted by the broken orange lines. A closer evaluation of the lath morphologies from the unetched backscattered (BSE) images of Fig. 2c shows more finely spaced laths for the Nb steel.

The NbMo steel displayed relatively wider and more bulgy laths as observed within a packet (red



**Figure 1** Experimental dilatation strain versus temperature profile showing  $M_s$  and  $M_f$  temperatures for both steels **a** full-range cooling profile, **b** enlarged region indicating transformation start and finish temperatures ( $M_s$ , martensite start,  $M_f$  martensite finish temperature).

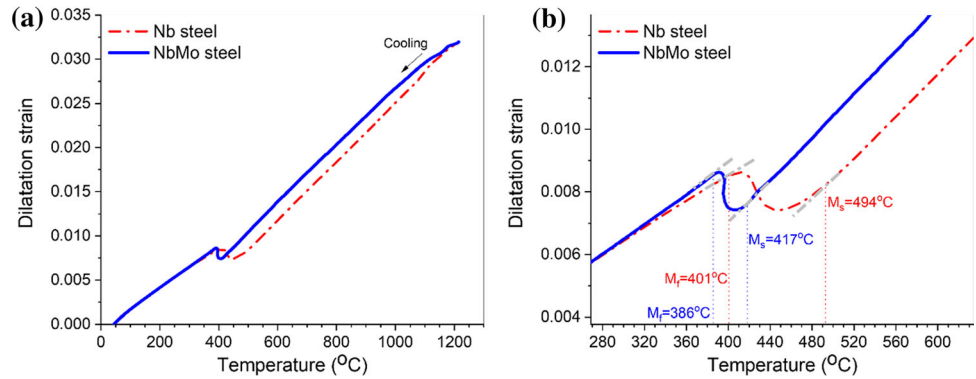
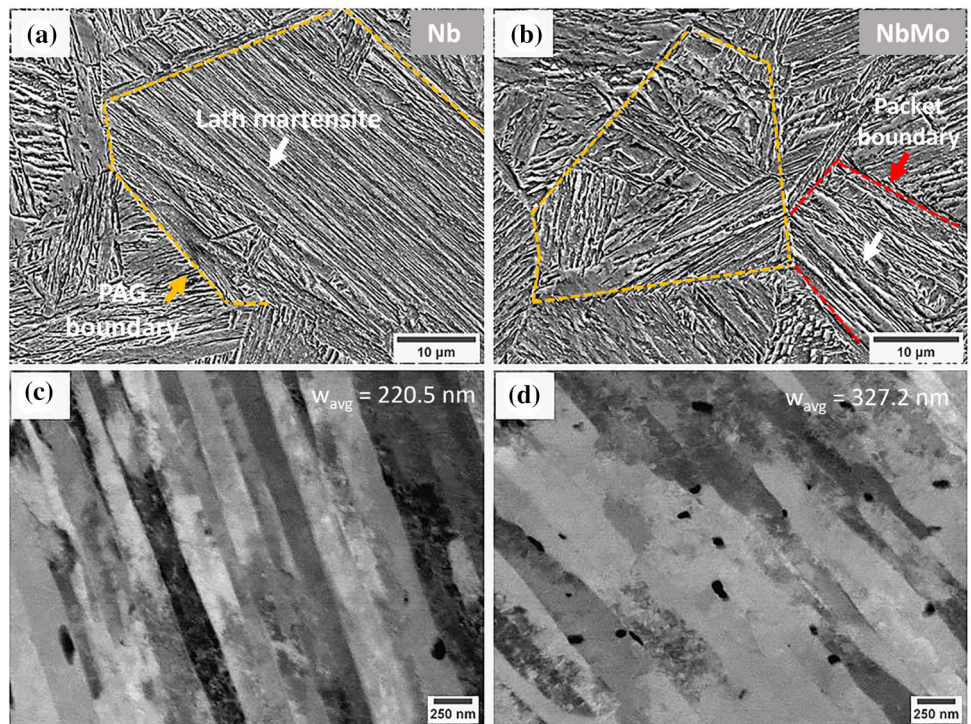


**Figure 2** SEM micrographs of as-quenched lath martensite (white arrows) microstructure observed using SE imaging for **a** the Nb steel, **b** the NbMo steel showing PAGs (boundaries in orange broken lines) and a packet boundary (red). The lath morphology observed using BSE imaging of regions indicated by white arrows from **a**, **b** showing finely spaced laths of **c** the Nb steel, and wider, bulged laths for **d** the NbMo steel. ( $w_{avg}$ : average lath width).



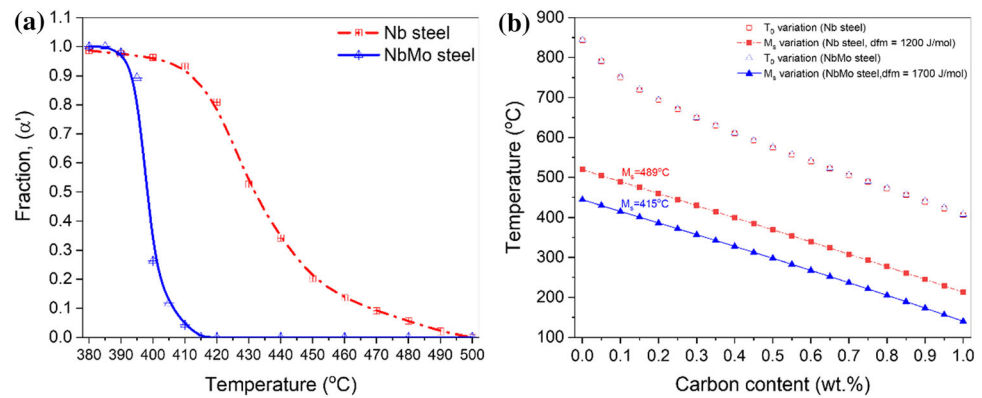
boundary) of laths shown in Fig. 2d. A quantitative estimate of the average lath width using the mean intercept method found average lath width values of 221 nm and 327 nm for the Nb and NbMo steels, respectively. The wider laths in the NbMo steel also showed higher tendency of intra-lath auto-tempered carbides (black dots inside laths, Fig. 2d). Similar carbides were rarely observed in the Nb steel while some indications of clustering were seen near lath boundaries. However, these features were too fine to be imaged precisely using SEM only.

### Initial martensite fraction estimation

To determine the martensite transformation kinetics during cooling between the  $M_s$  and  $M_f$  temperatures, the well-known lever rule [35, 40] was applied to the dilatometry data and is shown in Fig. 3a.

The early initiation of martensitic transformation in the Nb steel is evident from the plot in Fig. 3a which shows a steady increase in volume fraction of martensite at temperature  $< 495\text{ °C}$ . However, a sharp increase in the volume fraction of martensite for the NbMo steel is observed closer to 415 °C. The

**Figure 3** **a** Martensite volume fraction estimation using lever rule, **b** MatCalc simulated  $M_s$  variation with carbon content.



Nb steel approaches completion of the martensitic transformation earlier than the NbMo steel, but its transformation kinetics seems to gradually slow down below  $\sim 420$  °C. The same can be seen for the NbMo steel at temperatures below  $\sim 395$  °C.

The MatCalc thermokinetic simulation of  $M_s$  temperature for both the steels under varying C content is shown in Fig. 3b. The variation profiles of the  $T_0$  temperature with C content overlap for the two steels, which indicates a minor role of Mo in influencing the same. However, the simulations to estimate  $M_s$  variation for the same C content (0.1% C) resulted in remarkably close matches to dilatometry of 415 °C for the NbMo and at 489 °C for the Nb steels. These results highlight the role of Mo in lowering the  $M_s$  temperature even at same C content during quenching [41].

## Hierarchical microstructure evaluation

### Prior austenite grain size evolution

The EBSD inverse pole figure maps (IPF) of lath martensite as shown in Fig. 4a, b are overlaid with image quality (IQ) maps, while boundary misorientations between  $20^\circ$  and  $47^\circ$  were selected as PAGs based on similar analyses by Hidalgo et al. [11]. The boundary misorientations are based on the K-S orientation relationship between austenite and martensite. Previous reports on martensitic microstructures in low-C alloy steels [42] defined martensite boundaries with misorientations of  $10^\circ$ – $20^\circ$  and  $47^\circ$ – $57^\circ$  as packets and  $50^\circ$ – $60^\circ$  as blocks. Therefore, it is presumed that misorientations in the misorientation range between these features must be assigned to prior austenite grain boundaries. The scans show well-developed PAG units with similar colored martensite laths sharing identical crystal orientations

arranged into blocks. The degree of lath orientation variation within blocks appears to be more prominent in the Nb (Fig. 4a) as compared to the NbMo steel. A closer examination of the prior austenite grains was achieved via parent microstructure reconstructions from the same EBSD maps.

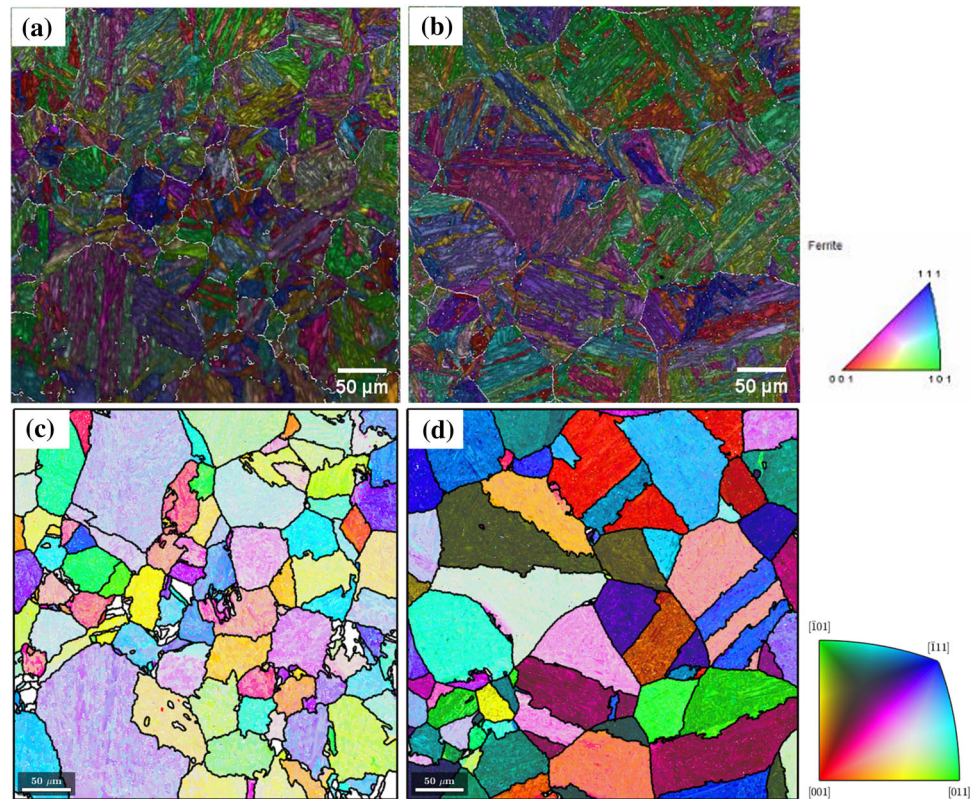
The PAG reconstructions along with parent grain orientations are shown in Fig. 4c, d. The colored representation of the individual parent grains is shown along with their grain boundaries in black. It is evident from the reconstruction maps that the NbMo steel exhibits coarser PAGs compared to the Nb steel although both steels were prepared and quenched under the exact same experimental conditions. Overall, PAGs in the Nb steel were mostly polygonal and smaller when compared to NbMo austenite grains. Interestingly, several reconstructed PAGs in the NbMo map exhibit annealing twins in the austenite. Such observation is frequent for low stacking fault phases like austenite during annealing of previously worked materials [19]. Such twin boundaries were discarded in subsequent PAG measurements. Multiple EBSD inverse pole figure (IPF) maps of both steels were used to assess average intercept grain size for the PAGs. While the Nb steel exhibited mean PAG size of 50  $\mu\text{m}$ , the NbMo steel exhibited a mean PAG size of 94  $\mu\text{m}$ .

### Packet and variants analysis

A more exhaustive analysis of the martensite packet and variant distributions in the child (martensite) microstructures was carried out using parent reconstruction generated output maps. Figure 5a, b shows packet ID distribution maps for both steels, revealing randomly distributed lath martensite packets wherein each color denotes a particular packet (of



**Figure 4** EBSD IPF map overlaid with image quality (IQ) map and misorientations boundaries (in white) between  $20^\circ$  and  $47^\circ$  for determination of PAG boundaries in **a** the Nb steel, **b** the NbMo steel. Parent austenite grain reconstruction using MTEX toolbox for **c** the Nb steel, **d** the NbMo steel.



four) formed from the same habit plane throughout the child microstructure. The reconstructions in certain areas remain incomplete. Such regions can be seen as white patches in the Nb steel maps. This is due to a parent–child orientation mismatch from the assumed KS orientation relationship which resulted in incomplete reconstruction around those regions. The packet distribution showed randomly distributed packet IDs for both maps with a common trend of exhibiting multiple packet IDs verifiable by the presence of multiple color shades of packets within smaller parent austenite grains.

Extension of this analysis to lath variant ID distribution maps along with martensite grain boundaries are shown in Fig. 5c, d. Evidently, the lath variants represent lath martensite blocks while each individual block consists of pairs of two variants out of the possible 24. This variant pairing was done according to the classification among common Bain groups often seen in lath martensitic steels [6, 12]. While the map only shows the individual variant IDs, a closer examination revealed a greater number of variants being formed within finer PAGs, just like the trend observed for the packet IDs in both steels.

For a better illustration of the frequency of individual variants within individual PAGs, parent

grains were selected from the variant distribution maps for each steel using the interactive grain analysis function in the MTEX-OR tool script. The results from individual parent grains outlined in white boundaries from both variant maps in Fig. 5c, d are shown in Fig. 6a, b, where evidently more variants are observed to have been formed inside selected PAGs in the Nb steel compared to the NbMo steel.

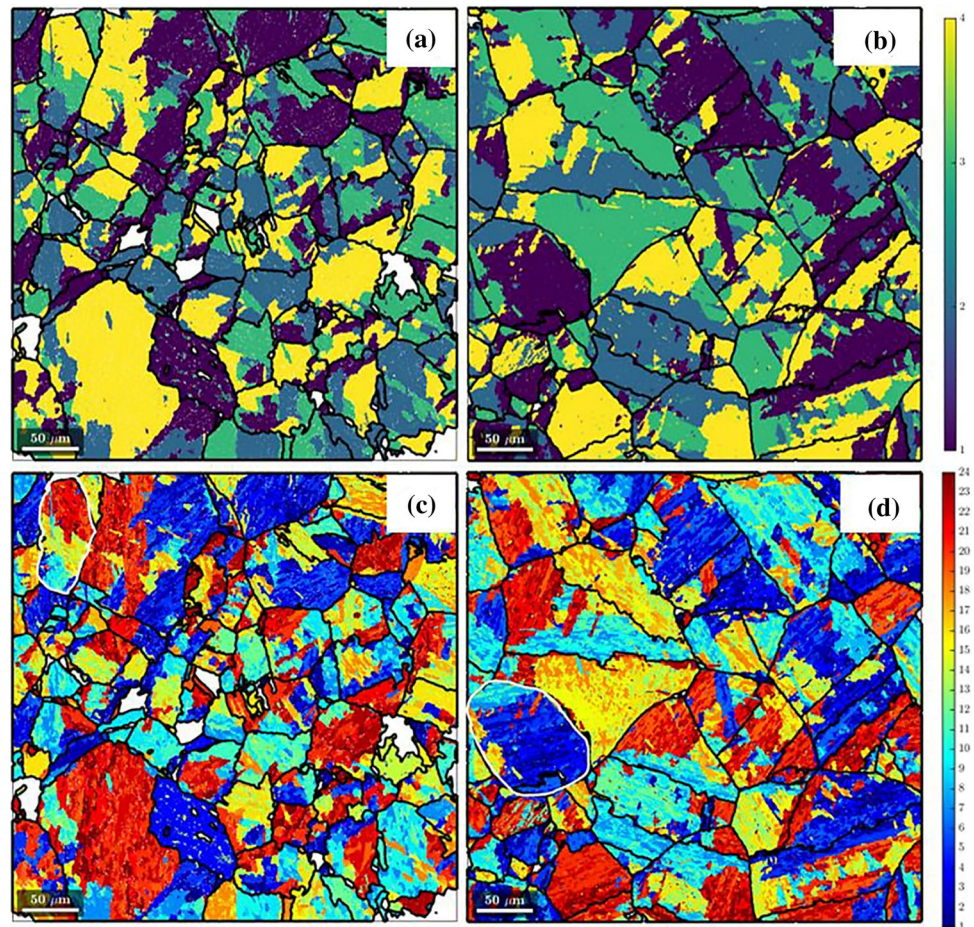
Similarly, higher-variant-frequency distributions for the Nb steel compared to the NbMo steel were recorded for several other parent grains but only one representative case is shown here. A quantitative confirmation through area normalized frequency distribution plots of all 24 possible variants forming inside selected PAGs in both the steels is shown in Fig. 6c, d. Almost all possible 24 lath variants except variants V2 and V5 are present within the analyzed Nb parent grain. However, the NbMo grain showed limited numbers of variants, mostly variants between V1 and V8.

#### *Hierarchical unit size evaluation*

The EBSD data analysis was further extended to study the average block width following an approach reported by Ueji et al. [43] for as-quenched lath



**Figure 5** MTEX constructed child (martensite) packet distribution maps for **a** the Nb steel, **b** the NbMo steel, and variant distribution maps for **c** the Nb steel, **d** the NbMo steel. Corresponding color legends indicate the respective packet and variant IDs of martensite.



martensite. Assuming a KS orientation relationship between parent and child microstructures, misorientations in the range of  $50^{\circ}$ – $60^{\circ}$  were defined as block boundaries within individual PAGs from IPF maps [11]. Multiple PAGs were cropped from the entire scanned datasets for individual analyses, wherein block boundaries were overlaid over the cropped PAG IPF maps as shown in Fig. 7a, b. The solid black lines represent block boundaries.

For validation of the analyzed hierarchical features from the cropped PAGs to be essentially from single parent grains, experimental  $\{101\}_{\alpha}$  ferrite pole figures were assessed as shown in Fig. 7c, d. The experimental pole figures correspond to similar observations for parent grain pole figures made previously by Hidalgo et al. [11].

The overall length of block boundaries was recorded from the analyzed PAGs from the cropped parent grain IPF map for both steels. The image analysis tool ImageJ was then used to determine the total cropped area for all investigated PAGs. Assuming

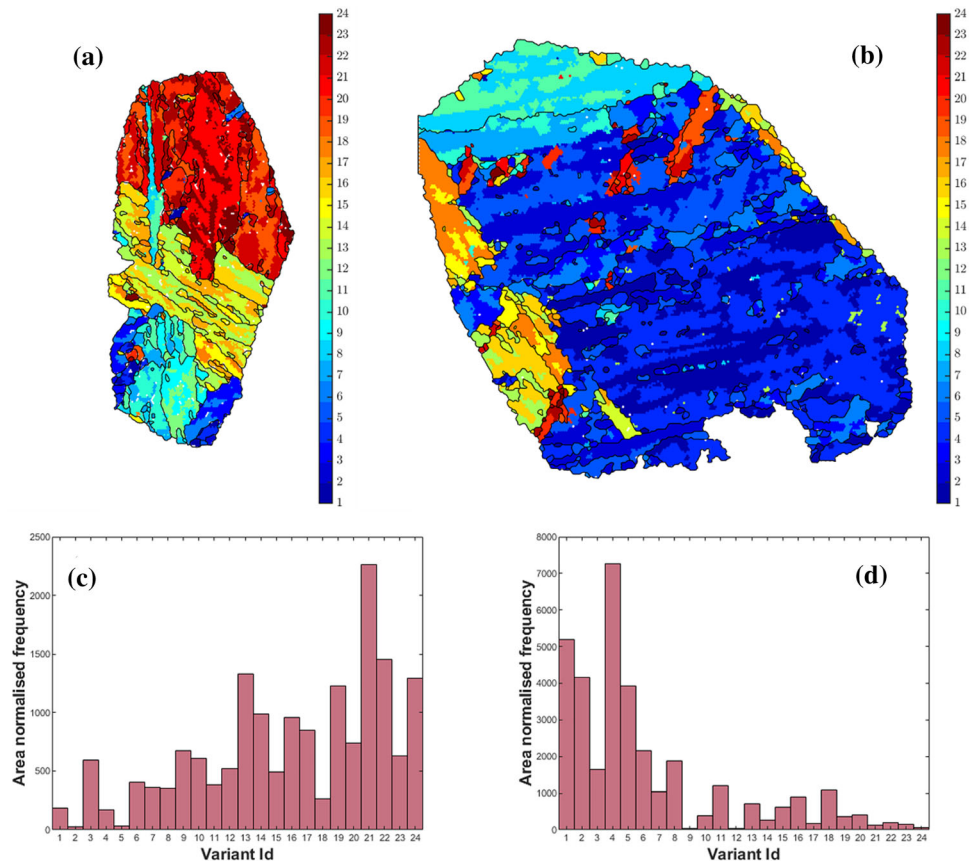
the measured scan area being representative of the three-dimensional morphology of the martensite substructure, the total area of block boundaries per unit volume  $S_V$  was calculated for each individual PAG by dividing the measured cropped area from the total block boundary length. Next, the block width as a measure of the mean intercept length ( $L$ ) was determined using the simple relationship for three-dimensional shape of masses [43].

$$S_V = 2/L \quad (1)$$

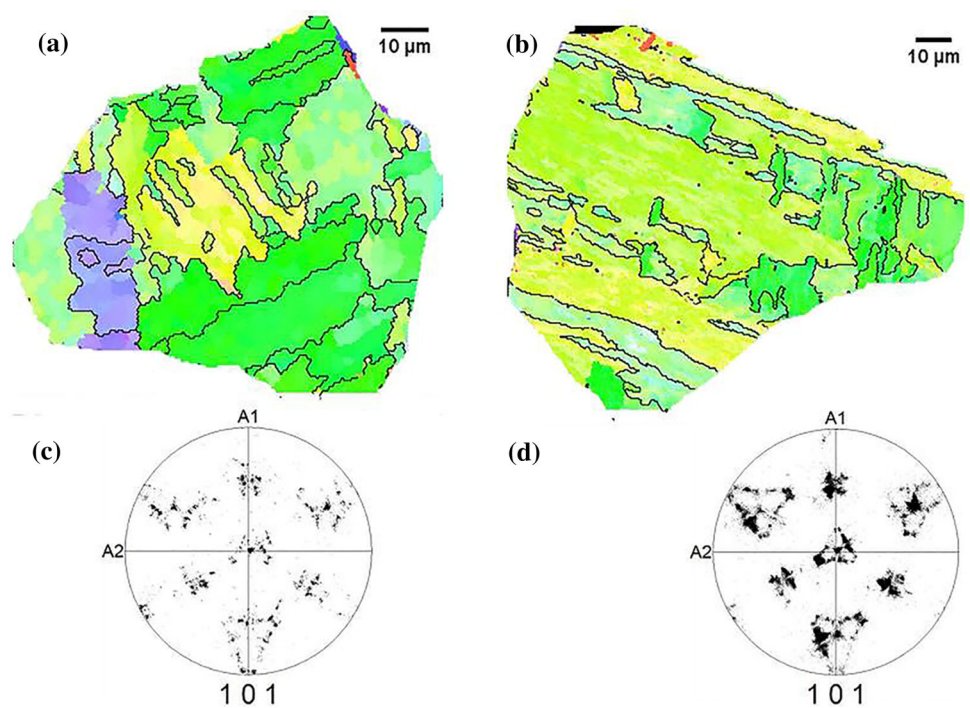
Additionally, boundary misorientations in the ranges of  $10^{\circ}$ – $20^{\circ}$  and  $47^{\circ}$ – $57^{\circ}$  were selected as packet boundaries. To evaluate their sizes via the mean intercept length method, misorientation line profiles along the width of the units were drawn across each pre-defined misorientation area. The evaluation of the packet size and block width along with the PAG sizes is shown in Fig. 8. The grain size plot clearly suggests that the evolving hierarchical units such as packets and blocks follow a similar trend to what was



**Figure 6** Martensite variants inside representative PAGs for **a** the Nb steel, **b** the NbMo steel, and frequency distribution of available variants inside selected PAGs for **c** the Nb steel, **d** the NbMo steel.



**Figure 7** Typical PAGs in **a** the Nb and **b** the NbMo steel in IPF coloring. Blocks of martensite laths of the same variants are shown in the same color, separated by high-angle block boundaries ( $50^{\circ}$ – $60^{\circ}$ ) shown as black solid lines. **c** and **d** Represent experimental  $\{101\}_{\alpha}$  pole figures depicting martensite crystal orientations inside **(a)** and **(b)** austenite grains, respectively.



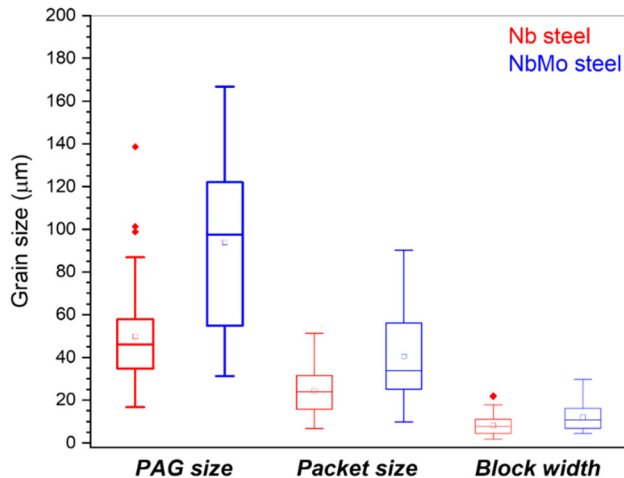


**Figure 8** Hierarchical unit sizes in as-quenched microstructure of Nb and NbMo steels.

seen in the PAG evaluation. The mean packet size was 24.3  $\mu\text{m}$  for the Nb steel, while it was 40.4  $\mu\text{m}$  for the NbMo steel. Mean block width values observed were 8.2  $\mu\text{m}$  and 11.9  $\mu\text{m}$  for Nb and NbMo steels, respectively.

## Lath substructure evolution

### *Nb steel lath substructure*

The typical site within a selected prior austenite grain for lift-out of a TEM lamella for the Nb steel is shown in Fig. 9a. A low-magnification image of the lamella is shown in Fig. 9b with two sets of parallel laths observed. One set is perpendicular to the sample surface and the other set is impinges at  $\sim 100^\circ$  to the vertical laths halfway down the sample. Within the set of horizontal laths, a higher-magnification BF-TEM image revealed the typical dislocation substructure inside laths with lath boundaries represented by broken lines in Fig. 9c.

Bright-field (BF) STEM imaging further revealed clusters of intermittently decorated precipitates (yellow arrows) along lath boundaries as highlighted in Fig. 9d. These precipitates were too fine to be reliably analyzed using STEM-EDS but are typical examples of auto-tempered Fe–C carbides forming along the boundaries given their size [22, 44]. Moreover, a qualitative estimate from an EDS mapping of the same region ruled out that particles were either Ga or Pt, a common artifact of  $\text{Ga}^+$  milling. The average diameter of the observed carbides in Fig. 9d was measured to be around 23 nm.

Further work on the chemical investigation of these extremely fine lath boundary carbides necessitates atom probe investigations which is part of an ongoing study. Interestingly, the Nb steel lath substructure contains intra-lath long and short twins close to the lath boundaries as shown in Fig. 9e, f. Notably, while the longer twins were frequently observed to run parallel to the lath boundaries, several shorter twins were also observed running across laths at certain angles and not necessarily parallel to the laths. Additional images of such twin observations for the Nb steel are provided in Supplementary Fig. 2.

Figure 9e also reveals the presence of clustering of auto-tempered carbides with mean diameters of  $\sim 4.4$  nm inside the region marked by the yellow, dashed ellipse. Additional clustering of fine carbides close to a lath boundary is indicated by the arrow in Fig. 9e. A magnified image of a cluster of short twins as indicated by the green rectangle in Fig. 9e is presented in Fig. 9f. Based on several such observations over multiple laths, both long and short twins were observed more frequently in proximity to impinging laths of differently oriented sets of laths. A selected area diffraction (SAD) pattern was recorded over an isolated short twin (inside a lath) shown in Fig. 9g with a boundary width of  $\sim 14$  nm. The SAD pattern from Fig. 9h revealed the presence of extremely fine precipitates within or close to the isolated short twin boundary. The average size of such precipitates (indicated by circles in Fig. 9g) is  $< 5$  nm. These precipitates were found to hold an orientation relationship at near  $[111]$  zone axis with the matrix near to  $[011]$ . The presence of faint streaking around diffraction spots (indicated by blue arrows) lines provides further indication of the presence of fine twins.

### *NbMo steel lath substructure*

Figure 10a shows a low-magnification image of the NbMo steel lift-out lamella with several sets of randomly distributed parallel sets of laths in multiple spatial orientations, as observed before for the Nb steel. Figure 10b represents multiple sets of laths with a common orientation closer to the edge of the lamella showing relatively wider laths. The region depicted inside of the white rectangle in Fig. 10b was further examined and is shown in Fig. 10c, wherein individual laths appear to show a high concentration



**Figure 9** **a** SEM micrograph of typical region selected for the FIB lift-out from the Nb steel, **b** BF-TEM micrograph showing the corresponding lamella, **c** dislocations as lath substructure, **d** BF-STEM image revealing segregation of auto-tempered carbides (marked by yellow arrows) along lath boundaries, **e** intra-lath long and short twins with fine clusters of auto-tempered carbides as indicated by dashed, yellow ellipse and build-up of several clusters as indicated by the arrow, **f** magnified region with short twins from **e**, **g** HR-TEM observation of a short twin with neighboring fine precipitates (as indicated by the green circles), **h** selected area diffraction (SAED) pattern over the region shown in **g** with diffused streaking between spots as marked by blue arrows, indicating a twin.

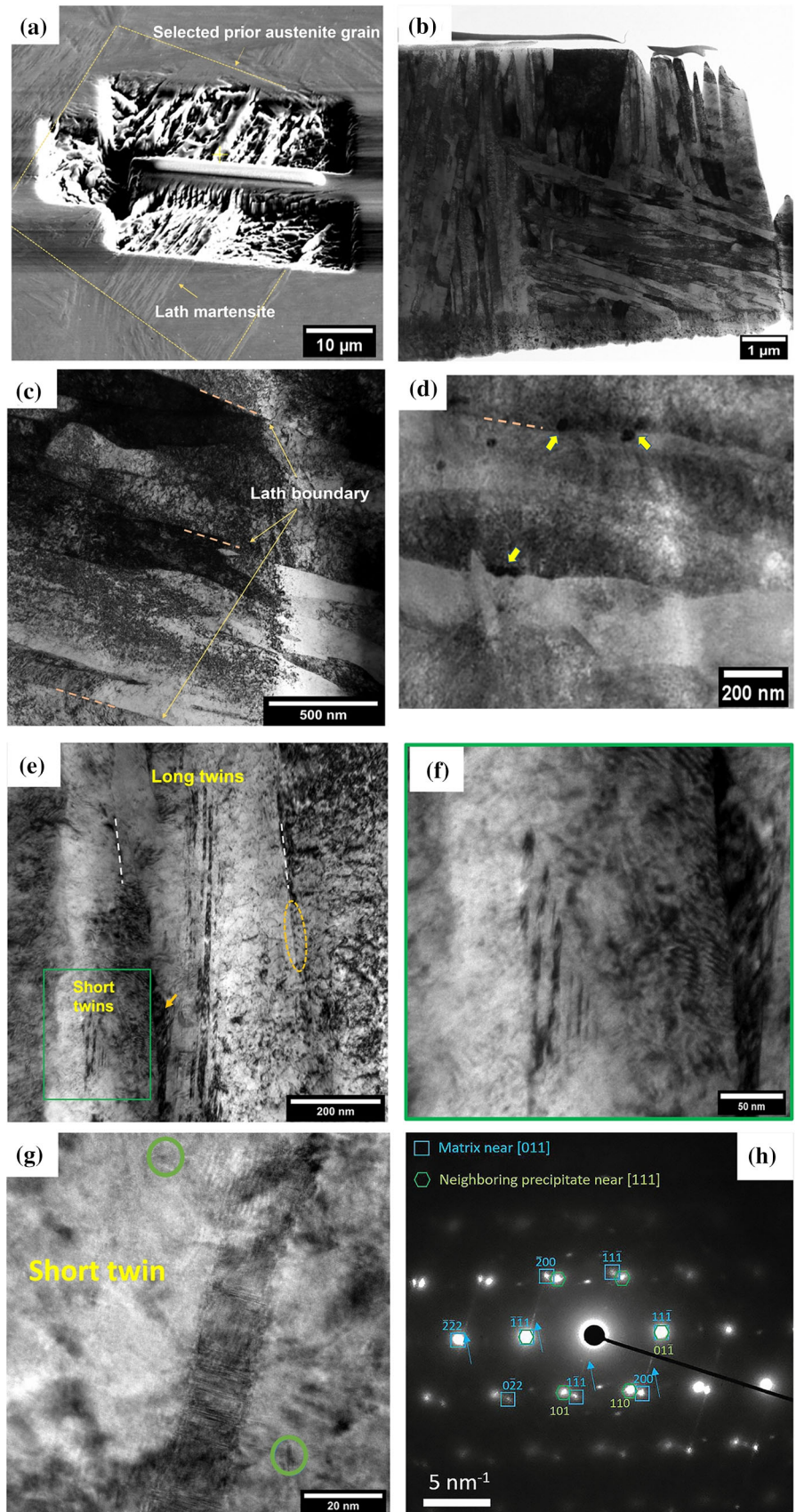
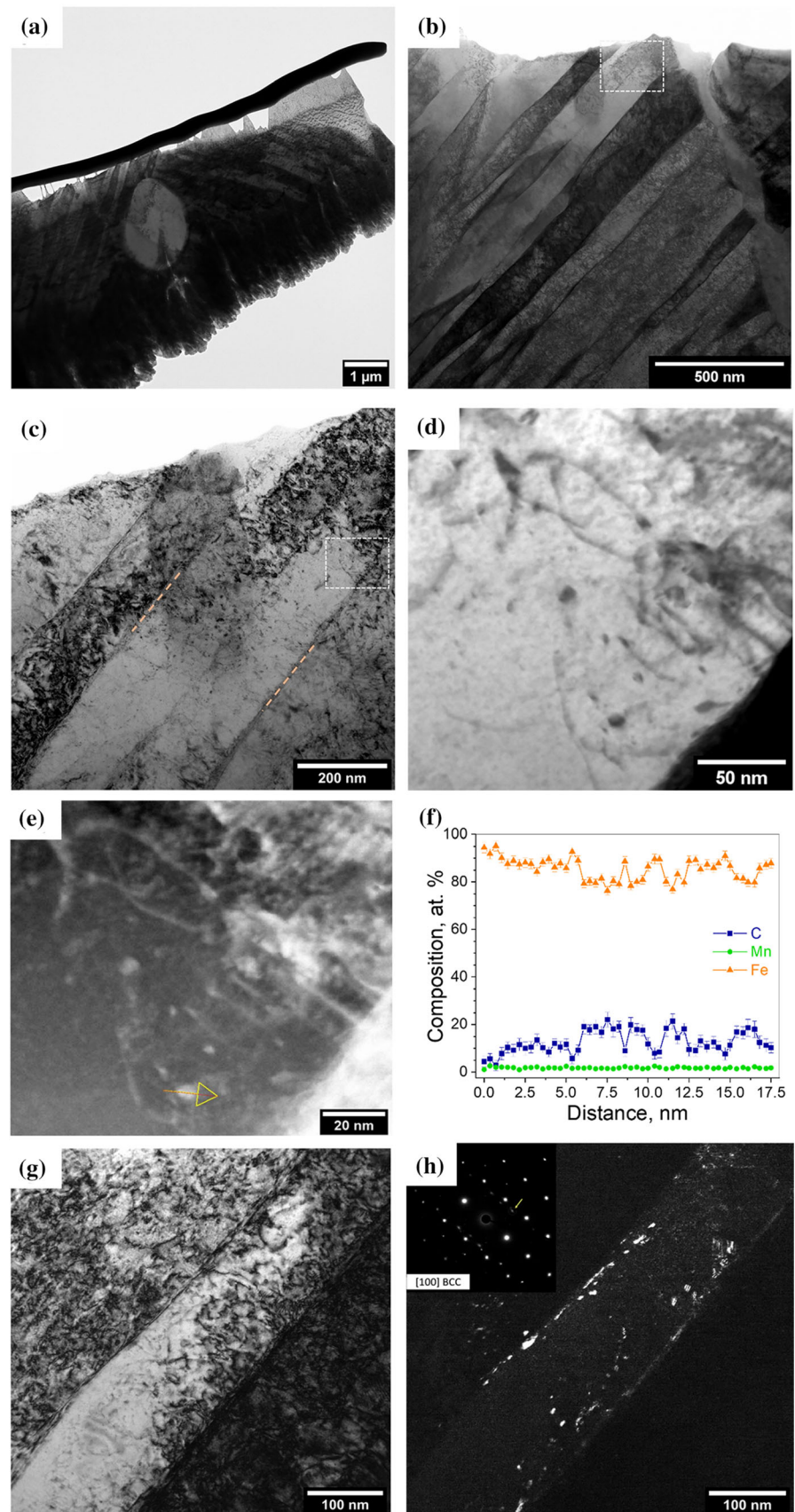




**Figure 10** **a** Bright-field TEM micrograph of the NbMo steel lift-out lamella, **b** relatively wider lath morphology observed in this lamella, **c** higher-magnification region of a lath close to edge of the lamella with lath boundaries (in orange broken lines), **d** prominent dislocation auto-tempered carbide interaction, **e** dark-field STEM image of region **d** showing fine auto-tempered precipitates in the vicinity of dislocations, **f** EDS line scan of selected precipitates seen in **e** showing Fe–C carbides, **g** bright-field TEM image of a fine lath, **h** corresponding dark-field image revealing the presence of intra-lath platelike carbides along with spherical lath boundary segregation with inset showing selected area diffraction along the [100] bcc zone axis with arrow indicating spot used to record the DF image.



of entangled dislocations near to the lath boundary while the center region remain relatively dislocation-free.

A higher-magnification image closer to the lath boundary is shown in Fig. 10d, revealing fine intra-lath auto-tempered carbides in the vicinity of fine threadlike dislocation entanglements. Corresponding dark-field STEM images were recorded which further confirm this substructure contrast as consistent with fine auto-tempered nano-sized carbides near dislocations as were observed previously in [25].

Chemical investigation of the observed fine carbides using EDS line scanning over a selected particle is shown in Fig. 10e. The composition profile presented in Fig. 10f shows the investigated precipitate to be close to  $15 \pm 2.6$  at. % which is below stoichiometric C content in cementite. The relatively higher Fe content is due to the carbide being surrounded by the Fe matrix which will skew the composition measurement. The average size of several other intra-lath precipitates observed within the dislocation entanglement region in the vicinity of lath the boundary varied between  $\sim 2$  and 15 nm in diameter.

Further examination of neighboring laths with more pronounced dislocation substructures is shown in the bright-field image in Fig. 10g. The corresponding DF image, however, helped to confirm the presence of intra-lath carbides as shown in Fig. 10h. Choosing a weak diffraction spot as indicated by the arrow inside the inset image of the recorded SAD pattern along a [100] bcc zone axis in Fig. 10h confirmed the presence of both extremely fine intra-lath platelet-like and possible decoration of extremely fine carbides along the lath boundary. This also demonstrates that there is a structural relationship between the carbides and the matrix. The NbMo steel, however, did not reveal twinning as was seen previously in the Nb steel, not even after multiple attempts of tilting to change diffraction conditions to near the {110} zone axis. Additional TEM micrographs confirming the absence of twins in multiple laths from different regions are provided in Supplementary Fig. 3.

## Discussion

### Hierarchical microstructure evolution

The results presented here provide evidence for the dependence of hierarchical microstructural subunits

in lath martensite on the PAG size. A finer PAG size in the Nb steel (Fig. 4c, d) led to the evolution of finer blocks (see Fig. 8) and lath widths (Fig. 2c, d) compared to slightly coarser PAGs seen in the NbMo steel. Hidalgo et al. [11] previously observed similar refinements of packet and block widths upon multiple quenching and reheating cycles from 800 °C post-initial austenitization at 1100 °C for 180 s which led to overall refinement of the PAG size in a 0.3C–1.6Si–3.5Mn steel. The tendency of finer austenite grains to form greater numbers of blocks and packets was also studied by Prawoto et al. [45] in medium-C steels for average PAG sizes between 52 and 200  $\mu\text{m}$ . The increased tendency of block formation in the Nb steel with finer PAGs also led to more closely spaced blocks with more block boundaries. These interfaces are barriers to dislocations, effectively strengthening the surrounding austenite regions during the transformation. As a likely consequence, the initial martensite formation caused higher transformation shear stresses, which additionally introduced a higher density of dislocations as substructures for accommodating these plastic strains. Nonetheless, existing packets and block boundaries also serve as obstacles to block growth which explains the relation between finer parent grain size and finer hierarchical substructures.

MTEX analyses of variant distribution maps showed the presence of almost all of the possible 24 variants, resulting in numerous intervariant boundaries and, hence, finer blocks in the Nb steel (Fig. 6c). The increasing tendency for formation of additional intervariant boundaries in lath martensite is known to promote grain refinement [4] while providing additional sites for the formation of clusters of fine auto-tempered carbides [15] as was observed for Nb lath boundaries in Fig. 9d. The retention of lath interfaces is an accompanying phenomenon of more pronounced boundary decoration with auto-tempered carbides during quenching. Similarly, the MTEX evaluation of the NbMo steel in Fig. 6d reveals that a coarser PAG size led to the evolution of more selective variants. The variant distribution map (Fig. 6d) showed higher population of certain variants (V1–V8). This could a possible explanation why relatively coarser laths are formed in the NbMo steel. The occurrence of bulgy and wider laths seen in the NbMo steel could be a direct result of fewer variants being formed due to coarser hierarchical

microstructure features allowing further lateral growth of laths.

These interfaces also act as barriers to dislocation glide, effectively strengthening the surrounding austenite regions during the transformation. As a likely consequence, after martensite formation, transformational shear stresses introduce dislocations to accommodate plastic strains. These dislocations pile up close to such interfaces. Thus, finer laths irrespective of the steel showed dislocations as lath substructures.

### Influence of $M_s$ temperature on the lath substructure evolution

The observed trends from Fig. 1 illustrate the influence of Mo in lowering of  $M_s$  temperature for the NbMo steel. This is expected as solute Mo is known to delay nucleation due to its preferential segregation to PAG boundaries during cooling [46]. Lath formation at higher  $M_s$  temperatures has been reported to be more prone to auto-tempering phenomena as commonly observed during quenching of low-C steels [47]. As a direct consequence, intra-lath substructures such as dislocations formed at higher  $M_s$  temperature tend to recover during cooling due to auto-tempering effects by self-migration to energetically favorable sites such as lath boundaries. Furthermore, solute C has a higher mobility at relatively higher  $M_s$  temperatures, allowing it to diffuse along these defect sites. Hutchinson et al. [25] have shown using atom probe tomography that C-rich planar features with average spacing of 130 nm exist along lath boundaries in a 0.12C–0.23Si–1.70Mn–0.014Nb–0.01Mo as-quenched steel. Similar observations were also reported for thermally activated diffusion processes leading to segregation of solute C and cementite to lower-energy sites such as lath boundaries in martensitic steels during tempering [48].

The inherently higher  $M_s$  temperature observed in the Nb steel would, hence, provide favorable thermal conditions for more pronounced lath boundary decoration with auto-tempered carbides. This would in turn lead to stronger pinning of the lath boundaries, thereby not allowing lateral growth of the laths, leading to finer lath widths. Although martensite formation is a nucleation-assisted event, recent studies have confirmed thermally activated growth phenomena of martensite laths, below  $M_s$  [49]. Consequently, the transverse (width) growth of laths

within blocks essentially depends on the nucleation of adjacent hierarchical units [50]. The affinity for pinning of lateral growth of laths during concurrent nucleation events is determined by the presence of lath boundary auto-tempered carbides and/or dislocation pile-ups at lath–lath interfaces according to the thermally activated growth model [14]. The mobility of excess solute C in fresh martensite will be higher at higher  $M_s$  temperature, promoting auto-tempering phenomena. It is therefore a valid assumption to expect the influence of lath boundary carbides in restricting the lateral growth of laths during rapid quenching of low-C Nb microalloyed steels.

Such fine segregation along lath boundaries is shown in Fig. 9d. While the observations in this study revealed clusters of precipitates along lath boundaries of  $\sim 23$  nm, the true sizes of these precipitates could be even smaller, beyond the resolution limits of the techniques applied here. Auto-tempered lath boundary carbides with a mean size of  $< 20$  nm were observed by Ping et al. [22] for 0.02C binary Fe–C alloys when samples were oil-quenched after austenitization at 1200 °C for 1 h.

A comparatively lower  $M_s$  temperature would reduce auto-tempering phenomena and provide fewer opportunities for defect recovery toward lath boundaries. Lowering the tendency for auto-tempering with lower  $M_s$  would enhance local availability of solute C within laths while additionally experiencing lower thermal mobility during the initial stages of martensite formation. A comprehensive study on water-quenched samples with auto-tempering in a 0.39C–1.6Si–0.6Mn–0.34Mo–0.7Cr steel by Badiner et al. [14] observed intra-lath dislocations enhancing precipitation kinetics by acting as heterogeneous nucleation sites while simultaneously reducing the precipitation kinetics near lath boundaries by lowering the amount and mobility of solute C. The combined conflicting precipitation kinetic effects would eventually lead to extremely fine sized intra-lath carbides in the vicinity of dislocation entanglements. The trapping of additional solute C within laths would effectively lead to reduced pinning of lath boundaries and segregation, encouraging lateral growth of laths. This explains the occurrence of bulgy laths in Fig. 2d. The laths in the NbMo steel as observed in Fig. 10d showed similar behavior when examined in the TEM with an overall wider



lath morphology and lower lath boundary segregation when compared to the Nb steel.

Moreover, wider laths have been reported to exhibit more frequent intra-lath carbides as seen in an earlier study by Thompson et al. [51] who observed fine rod-shaped  $\text{Fe}_3\text{C}$  precipitates within laths up to 150 nm in length and 15 nm width in a 0.4C–0.7Mn–0.3Si–1.7Ni–0.9Cr–0.2Mo steel that was quenched and tempered at 200 °C for ~ 60 min. The DF TEM in Fig. 10h in the present study shows similar platelets of fine intra-lath carbides for relatively coarser laths in the NbMo steel.

### Auto-tempered carbide size simulations

A quantitative estimate of the sizes of as-quenched auto-tempered carbides was attempted using MatCalc due to limitation of microscopy techniques used here. The simulations were performed keeping in mind the morphological variations where the auto-tempered carbides in Nb steel appeared to be more spherical (Fig. 9d), while platelet-shaped intra-lath carbides alongside spherical precipitates closer to lath boundary were observed in the NbMo steel (Fig. 10h). For this purpose, additional shape criteria were incorporated into the simulation of intra-lath nucleating cementite for the NbMo steel with a shape factor of 0.3 versus more spherical carbides with a shape factor value of 0.5 following similar studies on tempered cementite particles by Zamberger et al. [37]. Additionally, to simulate the higher dislocation interaction with solute C in the NbMo steel, the diffusion coefficient of the alloying elements along these sites was enhanced by a factor of 2.

The simulated auto-tempered carbide size distribution histograms for a representative volume element of precipitates nucleating on lath boundaries and on dislocations is shown in Fig. 11. It is in good agreement with experimentally observed precipitate sizes. It is interesting to note that the Nb steel with finer lath widths showed exceedingly higher counts of auto-tempered carbides in the size class between 0.5 and 5 nm. Similar sized precipitates were also observed close to a short twin inside lath for Nb steel (see Fig. 9g).

The tendency for intermittent lath boundary segregation observed in the Nb steel in Fig. 9d could be a result of clustering of such fine carbides along lath as reported in Fig. 1b. Moreover, the possibility of such extremely fine particles could also indicate the

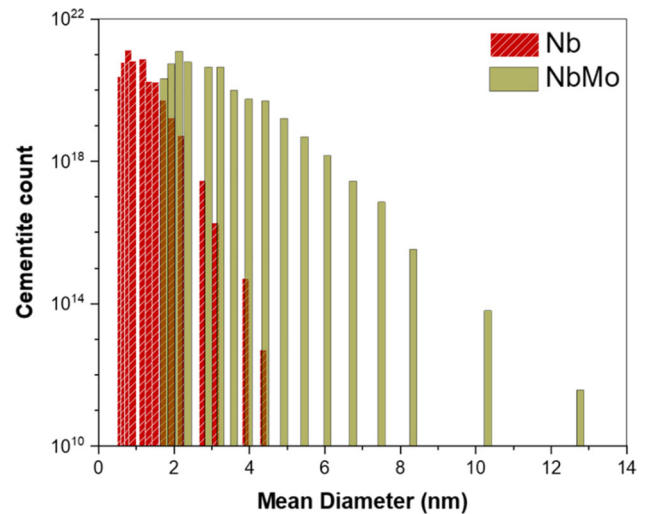


**Figure 11** MatCalc simulation of dislocation and subgrain boundary nucleating cementite size distributions in both steels.

formation of dynamically unstable  $\omega$ -Fe(C). While characterization of such particles is beyond scope of the current study, extremely fine precipitates near the short twin micrograph (see Fig. 9g, h) region were observed using HR-TEM. The reader is referred to Supplementary Fig. 4 for a characteristic image from the current study as evidenced by Moire interference.

Experimental TEM observations of fine platelet-shaped intra-lath carbides are confirmed by the simulations with a wider spectrum of precipitate size distributions between 2 and 13 nm for the NbMo steel, owing to a shift in their aspect ratio with varying precipitate morphologies. The nature of transition in the auto-tempered carbide morphologies with slight variation in the overall lath widths is thus verified.

### Lath substructure: twinning evolution

Laths in the Nb steel exhibited in-lath short and long twins in the current study. Similar lath martensite twin substructures after quenching were reported by Man et al. [24] post-austenitization between 1200 and 1300 °C in a Fe–0.2C alloy. They further reported transition of in-lath twin substructures to dislocation-like contrast during an in situ tempering treatment. They proposed a similar approach to study the role of auto-tempering (due to higher  $M_s$ ) phenomena during quenching toward promotion of similar detwinning phenomena in lath substructures. In the present study, while lath formation in the Nb steel with a higher  $M_s$  temperatures was more prone to auto-

tempering effects, some laths retained internal twins. A possible reason is believed to be the presence of extremely fine carbides as confirmed from TEM studies in the current study (see Fig. 9g, h). This observation, however, is contradictory to previous studies [8, 13, 24] claiming to observe in-lath twins as substructures only in martensites with lower  $M_s$ . Studies on Fe–Cr–C–Co steels by Raghavan et al. [52] observed that although Co inherently increases the  $M_s$  temperature, it yet led to repeated sighting of twinned martensite, thus exploring the possibility of achieving martensite twins at higher  $M_s$  temperature due to alloying influences in a medium-C quenched and tempered steel.

A different view on the origin of in-lath twins as substructure has recently received a lot of attention. Detailed work on twinned laths in ultra-low- to low-C binary Fe–C steels by Ping et al. [23] reported extremely fine dynamically unstable  $\omega$ -Fe(C) particles at twin boundaries after rapid quenching. It is critical to highlight here that excess C atoms are believed to occupy interstitial sites in this  $\omega$ -phase at the twin boundary [23, 51, 53]. The energy gap between the  $\omega$  and bcc structures is extremely small; hence, detwinning during auto-tempering follows a transformation from  $\omega$  to bcc resulting in migration of  $\{112\} < 111 >$ -bcc-type twin boundaries [23]. Another study on metastable  $\omega$ -Fe(C) particles by Ping et al. [22] observed supersaturation of solute C atoms during rapid quenching, leading to stabilization of these extremely fine particles at the  $\{112\} < 111 >$ -bcc-type twin boundaries.

The simulation of auto-tempered carbide formation during quenching from Fig. 11 underpins the presence of such fine precipitates in the current study. They could possibly be unstable  $\omega$ -Fe(C) particles, thus supporting the observed twinning phenomena in the Nb steel. An in-depth analysis of auto-tempering induced detwinning effect on short and long twin boundaries is explained in detail [22]. The authors explain how auto-tempering leads to migration of both types of twin boundaries. While the long twins eventually merge with lath boundaries, the complete detwinning of short twins results in carbides getting entangled with dislocations inside laths.

The simulated carbide size distribution for the NbMo steel in Fig. 11 shows significant counts of fine carbides across multiple size classes. This could be the result of detwinning induced transformation of the  $\omega$ -Fe(C) particles to platelet-shaped intra-lath

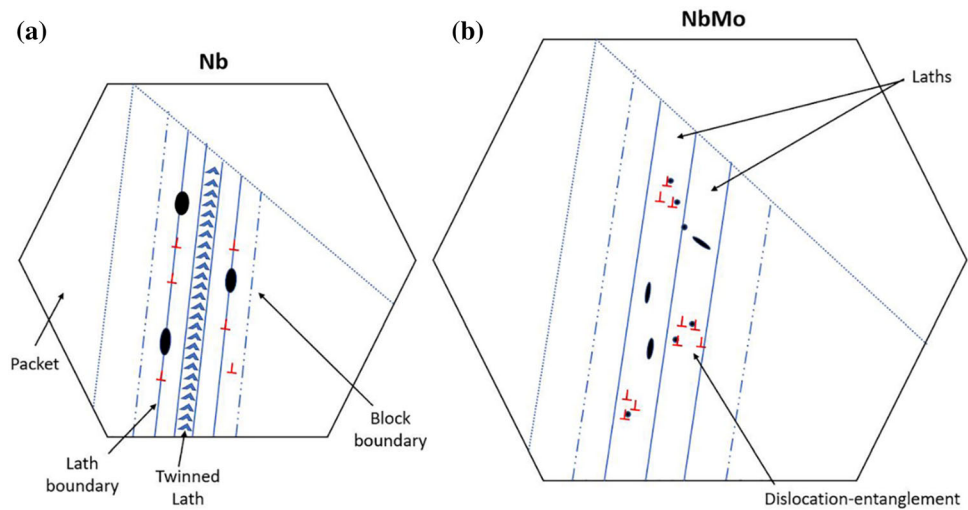
carbides. It is interesting to mention that laths in the NbMo steel did not exhibit twinning; thus, it can be concluded that the detwinning process must be more pronounced in this case. This may have resulted in the observed coarsening of laths (Fig. 10c) and the presence of intra-lath carbides as shown also in Fig. 9h. Although the absence of twinning in the NbMo steel can be explained based on pronounced detwinning phenomena, it is important to highlight that the  $M_s$  temperature of 417 °C is comparatively lower than that of the Nb steel at 494 °C. This translates into lower mobility of lath martensite defects such as dislocations. The likelihood of excess intra-lath defects locked inside the laths eventually promotes remaining solute C to form carbides in the vicinity of dislocation strain fields.

### Microstructural model

A schematic representation of the martensite substructure evolution in the two steels is shown in Fig. 12. This schematic encompasses all the features observed from the comprehensive microstructural characterization presented. Figure 12a shows finer hierarchical units starting from parent austenite grains, packets and blocks translating into finer laths in the as-quenched Nb steel. Individual laths exhibit internal twins alongside with dislocations in the vicinity of lath boundaries that are also decorated with clusters of fine auto-tempered carbides or unstable  $\omega$ -Fe(C) particles.

Figure 12b shows the martensite substructure evolution in the NbMo steel, where the hierarchical units are coarser, eventually leading to relatively wider laths. Individual laths display the presence of intra-lath dislocations and dislocation entanglements. Moreover, spherical and platelet-like intra-lath carbides were found. The presence of such intra-lath precipitates is believed to be a direct result of more pronounced detwinning phenomena leading to a transition of twin boundaries leaving carbides behind during to auto-tempering. No remaining twinned substructures were found in this steel. It is reasonable to suggest the influence of Mo in lowering of the  $M_s$  temperature eventually led to the evolution of the coarser hierarchical units while also limiting solute C mobility.

**Figure 12** Schematic illustration of lath substructure evolution in **a** the Nb steel and **b** the NbMo steel.



## Conclusions

A detailed examination of the lath martensite substructure evolution in two model microalloyed as-quenched low-carbon steels, a 0.1C–0.04Nb (Nb steel) and a 0.1C, 0.23Mo–0.05Nb (NbMo steel) is provided using correlative microscopy underpinned by MatCalc modeling. Novel observations around the hierarchical microstructural evolution during quenching of microalloyed steels and the influence of Mo addition can be summarized as follows:

- (1) Experimental dilatation quenching experiments supported by thermokinetic simulations revealed higher  $M_s$  temperatures of 494 °C for the Nb steel compared to 417 °C for the NbMo steel. As a result of this, EBSD studies revealed finer average hierarchical units with average PAG sizes of 50  $\mu\text{m}$  for the Nb steel and 94  $\mu\text{m}$  for the NbMo steel. Similarly, finer blocks at 8.2  $\mu\text{m}$  and 11.9  $\mu\text{m}$  for the Nb and NbMo steel, respectively, were observed.
- (2) MTEX-assisted parent reconstructions showed the evolution of more lath variants in finer blocks in the Nb steel and comparatively fewer lath variants in coarser blocks in the NbMo steel. Additional interfaces between variants in the Nb steel are believed to eventually restrict lateral growth of laths while increasing the tendency for clustering of auto-tempered carbides.
- (3) Site-specific TEM studies of martensite laths in the Nb steel confirmed the presence of dislocations, lath boundary clustering of extremely

fine auto-tempered carbides, and short and long twins as predominant substructures. The potential presence of fine and dynamically unstable  $\omega$ -Fe(C) particles cannot be ruled out as thermokinetic simulations using MatCalc showed high counts of fine precipitates in size class of 0.5 to 5 nm diameter commonly associated with formation near twin boundaries.

- (4) Conversely, the NbMo showed intra-lath interactions between extremely fine spherical carbides in the vicinity of dislocation entanglements. Moreover, platelet-shaped intra-lath precipitates were also observed. No twins were observed as substructures. This is a result of extensive auto-tempering despite the relatively lower  $M_s$  temperature.

These results are believed to provide new insights into the strength of martensite in modern microalloyed steels.

## Acknowledgements

S. Primig is supported by the Australian Research Council DECRA (DE180100440) and UNSW Scientia Fellowship schemes. Mr. Majid Parvizi and Prof. Simon P. Ringer helped with casting the samples using their facilities at the University of Sydney. Dilatometry was carried out at Deakin University with the help of Drs. Thomas Dorin and Alireza Vahid. Dr. Carina Ledermueller (UNSW School of Materials Science & Engineering) prepared the site-specific TEM lamellae. The authors thank Dr. Simon



Hager for technical assistance and use of facilities supported by Microscopy Australia at Electron Microscope Unit at the Mark Wainwright Analytical Centre at UNSW. Discussions with Prof. Ernst Kozeschnik (Technical University of Vienna) on MatCalc results are acknowledged.

### Author contributions

AC designed the study, carried out experiments and modeling, evaluated the data and wrote the manuscript. RW conducted TEM studies, evaluated the data and edited the manuscript. SP acquired the funding, did the supervision, and edited and wrote the manuscript.

### Funding

Open Access funding enabled and organized by CAUL and its Member Institutions.

### Data availability

The raw/processed data required to reproduce these findings cannot be shared at this time as the data also forms part of an ongoing study.

### Declarations

**Conflict of interest** The authors declare no conflict of interest.

**Supplementary Information:** The online version contains supplementary material available at <http://doi.org/10.1007/s10853-022-07275-9>.

**Open Access** This article is licensed under a Creative Commons Attribution 4.0 International License, which permits use, sharing, adaptation, distribution and reproduction in any medium or format, as long as you give appropriate credit to the original author(s) and the source, provide a link to the Creative Commons licence, and indicate if changes were made. The images or other third party material in this article are included in the article's Creative Commons licence, unless indicated otherwise in a credit line to the material. If material is not included in the article's Creative Commons licence and your intended use is

not permitted by statutory regulation or exceeds the permitted use, you will need to obtain permission directly from the copyright holder. To view a copy of this licence, visit <http://creativecommons.org/licenses/by/4.0/>.

**Supplementary Information:** The online version contains supplementary material available at <http://doi.org/10.1007/s10853-022-07275-9>.

### References

- [1] Sandvik BPJ, Wayman CM (1983) Crystallography and substructure of lath martensite formed in carbon steels. *Metallography* 16:199–227. [https://doi.org/10.1016/0026-0800\(83\)90005-8](https://doi.org/10.1016/0026-0800(83)90005-8)
- [2] Speich GR, Leslie WC (1972) Tempering of steel. *Metall Trans* 3:1043–1054. <https://doi.org/10.1007/BF02642436>
- [3] Maki T, Tsuzaki K, Tamura I (1980) The morphology of microstructure composed of lath martensites in steels. *Trans Iron Steel Insit Jpn* 20:207–214. <https://doi.org/10.2355/ijisinternational1966.20.207>
- [4] Kitahara H, Ueji R, Tsuji N, Minamino Y (2006) Crystallographic features of lath martensite in low-carbon steel. *Acta Mater* 54:1279–1288. <https://doi.org/10.1016/j.actamat.2005.11.001>
- [5] Morito S, Yoshida H, Maki T, Huang X (2006) Effect of block size on the strength of lath martensite in low carbon steels. *Mater Sci Eng A*. <https://doi.org/10.1016/j.msea.2005.12.048>
- [6] Stormvinter A, Miyamoto G, Furuhashi T, Hedström P, Borngenstam A (2012) Effect of carbon content on variant pairing of martensite in Fe-C alloys. *Acta Mater*. <https://doi.org/10.1016/j.actamat.2012.09.046>
- [7] Miyamoto G, Iwata N, Takayama N, Furuhashi T (2012) Quantitative analysis of variant selection in ausformed lath martensite. *Acta Mater*. <https://doi.org/10.1016/j.actamat.2011.11.018>
- [8] Krauss G, Marder AR (1971) The morphology of martensite in iron alloys. *Metall Trans* 2:2343–2357. <https://doi.org/10.1007/BF02814873>
- [9] Suikkanen PP, Cayron C, DeArdo AJ, Karjalainen LP (2011) Crystallographic analysis of martensite in 0.2C–2.0Mn–1.5Si–0.6Cr steel using EBSD. *J Mater Sci Technol*. [https://doi.org/10.1016/S1005-0302\(11\)60165-5](https://doi.org/10.1016/S1005-0302(11)60165-5)
- [10] Kinney CC, Pytlewski KR, Khachatryan AG, Morris JW (2014) The microstructure of lath martensite in quenched 9Ni steel. *Acta Mater* 69:372–385. <https://doi.org/10.1016/j.actamat.2014.01.058>

- [11] Hidalgo J, Santofimia MJ (2016) Effect of prior austenite grain size refinement by thermal cycling on the microstructural features of as-quenched lath martensite. *Metall Mater Trans A* 47:5288–5301. <https://doi.org/10.1007/s11661-016-3525-4>
- [12] Morito S, Tanaka H, Konishi R, Furuhashi T, Maki T (2003) The morphology and crystallography of lath martensite in Fe-C alloys. *Acta Mater* 51:1789–1799. [https://doi.org/10.1016/S1359-6454\(02\)00577-3](https://doi.org/10.1016/S1359-6454(02)00577-3)
- [13] Kehoe M, Kelly PM (1970) The role of carbon in the strength of ferrous martensite. *Scr Metall* 4:473–476. [https://doi.org/10.1016/0036-9748\(70\)90088-8](https://doi.org/10.1016/0036-9748(70)90088-8)
- [14] Badinier G, Sinclair CW, Sauvage X, Wang X, Bylik V, Gouné M, Danoix F (2015) Microstructural heterogeneity and its relationship to the strength of martensite. *Mater Sci Eng A* 638:329–339. <https://doi.org/10.1016/j.msea.2015.04.088>
- [15] Matsuda H, Mizuno R, Funakawa Y, Seto K, Matsuoka S, Tanaka Y (2013) Effects of auto-tempering behaviour of martensite on mechanical properties of ultra high strength steel sheets. *J Alloys Compd* 577:S661–S667. <https://doi.org/10.1016/j.jallcom.2012.04.108>
- [16] Ori OHM, Neycombe HO (1972) Tempering of a high carbon martensite\*. *Trans Iron Steel Inst Jpn* 12:112–117. <https://doi.org/10.2355/isiinternational1966.12.112>
- [17] Stormvinter A, Miyamoto G, Furuhashi T, Hedström P, Borgenstam A (2012) Effect of carbon content on variant pairing of martensite in Fe-C alloys. *Acta Mater* 60:7265–7274. <https://doi.org/10.1016/j.actamat.2012.09.046>
- [18] Li S, Zhu G, Kang Y (2016) Effect of substructure on mechanical properties and fracture behavior of lath martensite in 0.1C–1.1Si–1.7Mn steel. *J Alloys Compd* 675:104–115. <https://doi.org/10.1016/j.jallcom.2016.03.100>
- [19] Bhadeshia HKDH (2001) Modern bainitic alloys. In: *Bainite in steels: transformations, microstructure, and properties*, 2nd edn. IOM Communications, London
- [20] Tan YH, De Zeng C, Dong XC, He YH, Hu SQ (1992) New observation of martensitic morphology and substructure using transmission electron microscopy. *Metall Trans A* 23:1413–1421. <https://doi.org/10.1007/BF02647324>
- [21] Krauss G (1999) Martensite in steel: strength and structure. *Mater Sci Eng A* 273–275:40–57. [https://doi.org/10.1016/S0921-5093\(99\)00288-9](https://doi.org/10.1016/S0921-5093(99)00288-9)
- [22] Ping D, Liu T, Ohnuma M, Ohmura T, Abe T, Onodera H (2017) Microstructural evolution and carbides in quenched ultra-low carbon (Fe–C) alloys. *ISIJ Int* 57:1233–1240
- [23] Ping DH, Guo SQ, Imura M, Liu X, Ohmura T, Ohnuma M, Lu X, Abe T, Onodera H (2018) Lath formation mechanisms and twinning as lath martensite substructures in an ultra low-carbon iron alloy. *Sci Rep* 8:1–11. <https://doi.org/10.1038/s41598-018-32679-6>
- [24] Man TH, Liu TW, Ping DH, Ohmura T (2018) TEM investigations on lath martensite substructure in quenched Fe-0.2C alloys. *Mater Charact* 135:175–182. <https://doi.org/10.1016/j.matchar.2017.11.039>
- [25] Hutchinson B, Hagström J, Karlsson O, Lindell D, Tomberg M, Lindberg F, Thuvander M (2011) Microstructures and hardness of as-quenched martensites (0.1–0.5%C). *Acta Mater*. <https://doi.org/10.1016/j.actamat.2011.05.061>
- [26] Nanda T, Singh V, Singh V, Chakraborty A, Sharma S (2019) Third generation of advanced high-strength steels: processing routes and properties. *Proc Inst Mech Eng L*. <https://doi.org/10.1177/1464420716664198>
- [27] Zhao J, Jiang Z (2018) Thermomechanical processing of advanced high strength steels. *Prog Mater Sci* 94:174–242. <https://doi.org/10.1016/j.pmatsci.2018.01.006>
- [28] Spindler H, Klein M, Rauch R, Pichler A, Stiaszny P (2005) High strength and ultra high strength hot rolled steel grades—products for advanced applications. In: *1st international conference on super-high strength steels*
- [29] Bhole SD, Nemade JB, Collins L, Liu C (2006) Effect of nickel and molybdenum additions on weld metal toughness in a submerged arc welded HSLA line-pipe steel. *J Mater Process Technol* 173:92–100. <https://doi.org/10.1016/j.jmatprotec.2005.10.028>
- [30] Tang Z, Stumpf W (2008) The role of molybdenum additions and prior deformation on acicular ferrite formation in microalloyed Nb-Ti low-carbon line-pipe steels. *Mater Charact* 59:717–728. <https://doi.org/10.1016/j.matchar.2007.06.001>
- [31] Sun Z, Bei H, Yamamoto Y (2017) Microstructural control of FeCrAl alloys using Mo and Nb additions. *Mater Charact* 132:126–131. <https://doi.org/10.1016/j.matchar.2017.08.008>
- [32] Larzabal G, Isasti N, Rodriguez-Ibabe J, Uranga P (2017) Evaluating strengthening and impact toughness mechanisms for ferritic and bainitic microstructures in Nb, Nb-Mo and Ti-Mo microalloyed steels. *Metals* 7:65. <https://doi.org/10.3390/met7020065>
- [33] Chakraborty A, Primig S (2021) Influence of finish rolling temperature and molybdenum addition on strengthening of low carbon niobium steels—a computational and experimental study. *Steel Res Int*. <https://doi.org/10.1002/srin.202100085>
- [34] Kaar S, Steineder K, Schneider R, Krizan D, Sommitsch C (2021) New Ms-formula for exact microstructural prediction of modern 3rd generation AHSS chemistries. *Scr Mater* 200:113923. <https://doi.org/10.1016/j.scriptamat.2021.113923>

- [35] Gómez M, Medina SF, Caruana G (2003) Modelling of phase transformation kinetics by correction of dilatometry results for a ferritic Nb-microalloyed steel. *ISIJ Int* 43(8):1228–1237. <https://doi.org/10.2355/isijinternational.43.1228>
- [36] van Bohemen SMC, Sietsma J (2014) Kinetics of martensite formation in plain carbon steels: critical assessment of possible influence of austenite grain boundaries and autocatalysis. *Mater Sci Technol (United Kingdom)* 30:1024–1033. <https://doi.org/10.1179/1743284714Y.0000000532>
- [37] Zamberger S, Whitmore L, Krisam S, Wojcik T, Kozeschnik E (2015) Experimental and computational study of cementite precipitation in tempered martensite. *Model Simul Mater Sci Eng.* <https://doi.org/10.1088/0965-0393/23/5/055012>
- [38] Niessen F, Nyyssönen T, Gazder AA, Hielscher R (2021) Parent grain reconstruction from partially or fully transformed microstructures in MTEX. <https://arxiv.org/abs/2104.14603>
- [39] Tomus D, Ng HP (2013) In situ lift-out dedicated techniques using FIB-SEM system for TEM specimen preparation. *Micron* 44:115–119. <https://doi.org/10.1016/j.micron.2012.05.006>
- [40] Yang HS, Bhadeshia HKDH (2009) Austenite grain size and the martensite-start temperature. *Scr Mater* 60:493–495. <https://doi.org/10.1016/j.scriptamat.2008.11.043>
- [41] Yamada H, Sakurai T, Takenouchi T (1990) Effect of alloying elements on the peritectic temperature in low-alloy steels. *Tetsu-To-Hagane/Journal of the Iron and Steel Institute of Japan* 76:438–445. [https://doi.org/10.2355/tetsutohagane1955.76.3\\_438](https://doi.org/10.2355/tetsutohagane1955.76.3_438)
- [42] Karthikeyan T, Dash MK, Saroja S, Vijayalakshmi M (2015) Estimation of martensite feature size in a low-carbon alloy steel by microtexture analysis of boundaries. *Micron* 68:77–90
- [43] Ueji R, Tsuji N, Minamino Y, Koizumi Y (2002) Ultragrain refinement of plain low carbon steel by cold-rolling and annealing of martensite. *Acta Mater* 50:4177–4189. [https://doi.org/10.1016/S1359-6454\(02\)00260-4](https://doi.org/10.1016/S1359-6454(02)00260-4)
- [44] Ping DH, Ohnuma M (2018)  $\omega$ -Fe particle size and distribution in high-nitrogen martensitic steels. *J Mater Sci* 53:5339–5355. <https://doi.org/10.1007/s10853-017-1938-0>
- [45] Prawoto Y, Jasmawati N, Sumeru K (2012) Effect of prior austenite grain size on the morphology and mechanical properties of martensite in medium carbon steel. *J Mater Sci Technol* 28:461–466. [https://doi.org/10.1016/S1005-0302\(12\)60083-8](https://doi.org/10.1016/S1005-0302(12)60083-8)
- [46] Khare S, Lee K, Bhadeshia HKDH (2009) Relative effects of Mo and B on ferrite and bainite kinetics in strong steels. *Int J Mater Res* 100:1513–1520. <https://doi.org/10.3139/146.110222>
- [47] Ning D, Dai CR, Wu JL, Wang YD, Wang YQ, Jing Y, Sun J (2021) Carbide precipitation and coarsening kinetics in low carbon and low alloy steel during quenching and subsequently tempering. *Mater Charact.* <https://doi.org/10.1016/j.matchar.2021.111111>
- [48] Daigne J, Guttmannt M, Naylor JP (1982) The influence of lath boundaries and carbide distribution on the yield strength of 0.4% C tempered martensitic steels. *Mater Sci Eng.* [https://doi.org/10.1016/0025-5416\(82\)90176-8](https://doi.org/10.1016/0025-5416(82)90176-8)
- [49] Villa M, Hansen MF, Pantleon K, Somers MAJ (2015) Thermally activated growth of lath martensite in FeCrNiAl stainless steel. *Mater Sci Technol (United Kingdom)* 31:115–122. <https://doi.org/10.1179/1743284714Y.0000000583>
- [50] Levitas VI, Idesman A, Olson GB, Stein E (2002) Numerical modelling of martensitic growth in an elastoplastic material. *Philos Mag A* 82:429–462. <https://doi.org/10.1080/01418610208239609>
- [51] Thompson SW (2015) Structural characteristics of transition-iron-carbide precipitates formed during the first stage of tempering in 4340 steel. *Mater Charact* 106:452–462. <https://doi.org/10.1016/j.matchar.2015.05.030>
- [52] Raghavan M, Thomas G (1971) Structure and mechanical properties of Fe-Cr-C-Co steels. *Metall Trans* 2:3433–3439. <https://doi.org/10.1007/BF00703820>
- [53] Zhang P, Chen Y, Xiao W, Ping D, Zhao X (2016) Twin structure of the lath martensite in low carbon steel. *Prog Nat Sci: Mater Int* 26:169–172. <https://doi.org/10.1016/j.pnsc.2016.03.004>

**Publisher's Note** Springer Nature remains neutral with regard to jurisdictional claims in published maps and institutional affiliations.